

Detecting and monitoring long-term landslides in urbanized areas with nighttime light data and multi-seasonal Landsat imagery across Taiwan from 1998 to 2017

Tzu-Hsin Karen Chen^{a,b,c,*}, Alexander V. Prishchepov^c, Rasmus Fensholt^c, Clive E. Sabel^{a,b}

^aDepartment of Environmental Science, Aarhus University, Frederiksborgvej 399, DK-4000 Roskilde, Denmark

^bDanish Big Data Centre for Environment and Health (BERTHA), Aarhus University, DK-4000 Roskilde, Denmark

^cDepartment of Geosciences and Natural Resource Management (IGN), University of Copenhagen, DK-1350 København K, Denmark

Abstract

Monitoring long-term landslide activity is of importance for risk assessment and land management. Daytime airborne drones or very high-resolution optical satellites are often used to create landslide maps. However, such imagery comes at a high cost, making long-term risk analysis cost-prohibitive. Despite the widespread use of open-access 30m Landsat imagery, their utility for landslide detection is often limited due to low classification accuracy. One of the major challenges is to separate landslides from other anthropogenic disturbances. Here, we produce landslide maps retrospectively from 1998 to 2017 for landslide-prone and highly populated Taiwan (35,874 km²). To improve classification accuracy of landslides, we integrate nighttime light imagery from the Defense Meteorological Satellite Program (DMSP) and the Visible Infrared Imaging Radiometer Suite (VIIRS), with multi-seasonal daytime optical Landsat time-series, and digital elevation data from the Advanced Spaceborne Thermal Emission and Reflection Radiometer (ASTER). We employed a non-parametric machine-learning classifier, random forest, to classify the satellite imagery. The classifier was trained with data from three years (2005, 2010, and 2015), and was validated with an independent reference sample from twelve years. Our results demonstrated that combining nighttime light data and multi-seasonal imagery significantly improved the classification ($p < 0.001$), compared to conventional methods based on single-season optical imagery. The results confirmed that the developed classification model enabled mapping of landslides across Taiwan over a long period with annual overall accuracy varying between 96% and 97%, user's and producer's accuracies between 73% and 86%. Spatiotemporal analysis of the landslide inventories from 1998 to 2017 revealed different temporal patterns of landslide activities, showing those areas where landslides were persistent and other areas where landslides tended to reoccur after vegetation regrowth. In sum, we provide a robust method to detect long-term landslide activities based on freely available satellite imagery, which can be applied elsewhere. Our mapping effort of landslide spatiotemporal patterns is expected to be of high importance in developing effective landslide remediation strategies. Please find the published version at: <https://doi.org/10.1016/j.rse.2019.03.013>

Keywords: landslide recognition, nighttime light, Landsat, multi-seasonal imagery, long-term risk assessment, random forest, change detection, multi-sensor, spatiotemporal analysis

1. Introduction

From 1990 to 2017, landslides resulted in many casualties and caused roughly USD 4.5 billion of economic losses worldwide (EM-DAT 2018). Approximately 58% of deaths and 69% of economic losses occurred in East and Southeast Asia (EM-DAT 2018). East and Southeast Asia, one of the fastest urbanizing regions in the world, is currently experiencing rapid built-up area expansion (Schneider et al. 2015). Recent deadly events causing many thousands of casualties in densely populated regions, include the 2013 Uttarakhand landslides in India (183 persons/km²) (Martha et al. 2015), the 2008 Sichuan landslides in China (170 persons/km²) (Chigira et al.

2010) and the 2009 Kaohsiung landslides in Taiwan (445 persons/km²) (Tsou et al. 2011).

While in those regions the influence of population growth on landslide occurrence is inevitable (Petley 2010), historical landslide inventories are of great importance for supporting mitigation and adaptation strategies, such as monitoring landslide susceptible areas (Althuwaynee et al. 2012). Historical landslide maps that cover longer periods can characterize crucial spatiotemporal patterns of landslide activities. Cumulative occurrence of landslides, for instance, is considered as a predictor of landslides (Chuang and Shiu 2018). Other temporal characteristics, such as persistency, and reoccurrence rate after revegetation of former landslide sites, also reflect multiple factors such as the type and size of the landslide, the depths of the sliding plane, and the hydrogeological characteristics (Behling et al. 2014). Thus,

*Corresponding author

Email address: thc@envs.au.dk (Tzu-Hsin Karen Chen)

the knowledge gained from long-term landslide maps is useful for developing pathways for sustainable land use in landslide-prone areas (Fell et al. 2008).

However, historical landslide maps are largely unavailable because of mapping challenges. Mapping of landslide occurrence traditionally relies on field surveys and visual interpretation of aerial photos. Semi-automatic pixel-based and object-based image classification methods have also been developed to extract information about landslides from very high-resolution (VHR) satellite imagery (e.g., Quickbird, IKONOS, WorldView) (Hervás et al. 2003; Pradhan et al. 2016; Stumpf and Kerle 2011; Keyport et al. 2018). Studies have shown that object-based classification of images at <1m resolution, such as Quickbird and GeoEye-1, which utilize the geometry and texture of objects, can yield high overall accuracy (above 85%) in landslide mapping (Li et al. 2015; Stumpf and Kerle 2011). Nevertheless, retrospective mapping of landslide occurrence from VHR imagery is costly and does not allow tracing landslides before the late 1990s, when the first commercial VHR imagery became accessible. Repetitive observations with dense satellite time-series such as from Aqua/Terra MODIS at 250m resolution are cost-free but impose substantial limitations for detecting landslide due to the low spatial resolution.

In contrast, freely accessible medium-resolution satellite imagery, such as Landsat (30m) and SPOT (approximately 10m) imagery provide temporal coverage over several decades and are widely used to study land-cover change. Normalized Difference Vegetation Index (NDVI) and Normalized Difference Water Index (NDWI) derived from multispectral imagery are commonly used to differentiate rock-, soil-, and mud-covered landslides from vegetation and water bodies (Chen et al. 2013; Singh and Singh 2016; Chen and Lin 2018). However, Landsat-like imagery alone usually resulted in moderate classification accuracies (Barlow et al. 2003; Yu and Chen 2017). Even when geomorphological parameters derived from a digital elevation model (DEM) were used as ancillary data, the commission error and omission error for landslide detection can be as high as 30% (Hong et al. 2016; Yu and Chen 2017). The major challenge related to the use of Landsat-like multispectral imagery comes from the separation between landslides and the surrounding environment, as spectral signatures from landslide occurrences and anthropogenic landscapes are often similar. Human activities such as agricultural land use, forest clearcutting and constructions in hazard-prone zones in East and Southeast Asia, therefore, pose specific challenges regarding the accuracy of landslide detection (Borghuis et al. 2007; Martha et al. 2012).

Studies show that the applications of multi-temporal imagery can enhance land cover classification, such as fusing multi-date imagery, extracting time-series trajectories, and incorporating multiple seasonal features (Oetter et al. 2001; Guerschman et al. 2003; Khatami et al. 2016; Kennedy et al. 2010). Fusing multi-date

images can substitute missing information (e.g. clouds in optical satellite imagery) (Pohl and Van Genderen 1998). While many landslide mapping efforts were made on event-based bi-temporal change detection (Hölbling et al. 2015; Tsai et al. 2010; Rau et al. 2007), methods which use time-series imagery for monitoring ongoing processes have been developed in the past decade. For instance, NDVI time-series were used for adaptive change calculation, allowing the separation between permanently non-vegetated and post-event landslide areas in different geographic settings (Behling et al. 2014; Golovko et al. 2017). To monitor the geomorphological process of slow-movement landslides, time-series based optical imagery approaches have also been developed for retrieving surface displacements (Pham et al. 2018; Stumpf et al. 2017). Synthetic Aperture Radar interferometry (InSAR), known for its ability in dealing with atmospheric noise and monitoring deformation, was also found to perform better using time-series analysis of landslides (Hooper et al. 2012; Dong et al. 2018). However, time-series approaches require a high imagery frequency (Behling et al. 2016; Kennedy et al. 2010), imposing difficulties for long-term annual landslide mapping. While multi-seasonal Landsat images have been used for long-term land-cover mapping and change detection (Grădinaru et al. 2017; Makhmreh 2018; Prishchepov et al. 2012), their utility for constructing historical landslide maps are underexplored. We hypothesize that multi-seasonal imagery should improve classification accuracy, because landslides may occur or expand during the rainy season and expose bare soil while agricultural fields remains green.

We also hypothesize that ancillary nighttime light imagery could be applied to assess the spatial distribution of landslides. While optical imagery distinguishes landslide from vegetation, nighttime light data could separate landslide from anthropogenic activities interlinked with light use. Nighttime light data are tightly associated with population density, income level and economic activities (Doll et al. 2006; Jean et al. 2016). For instance, MODIS imagery combined with nighttime light data enhanced classification accuracy of urban areas (Sharma et al. 2016). Thus, we assume that by adding nighttime light data a classifier can better exclude such human activities from the areas affected by landslides, thereby overcoming the limitations of optical daytime reflectance data. The Defense Meteorological Satellite Program (DMSP) nighttime light data in combination with data from the more recent Visible Infrared Imaging Radiometer Suite (VIIRS) are available retrospectively, which combined with Landsat imagery provide a great potential to map landslides into the past. We are unaware of any studies that tested the suitability of nighttime light data to support automated landslide detection.

In this context, our major objective was to develop an automated approach for retrospective annual landslide mapping based on open-access satellite data

Table 1: Remote sensing variables used in this study and the spatial resolution of each dataset.

Metric	Description	Spatial resolution
Seasonal features	Seasonal mean values of winter, spring, and summer of bands (Blue, green, red, NIR, SWIR1, SWIR2), (Nichol and Wong 2005), NDVI (Martha et al. 2011), and NDWI (Wu et al. 2013), where $NDVI = \frac{NIR - red}{NIR + red}$ $NDWI = \frac{green - SWIR1}{green + SWIR1}$	30m
Slope	Degree values between 0 and 90 derived from DEM (Borghuis et al. 2007).	30m
Nighttime light data	Values rescaled to 0 (no light) – 63 (top luminosity)	about 900m (DMSP) about 450m (VIIRS)

(Landsat, DMSP and VIIRS) illustrated with data from landslide-prone Taiwan. We tested two hypotheses:

1. Whether using multi-seasonal imagery yields a statistically more accurate classification of landslides compared to single-season imagery, and
2. Whether adding nighttime light data results in a more accurate classification of landslides. Further, we evaluated the potential transferability of the developed model, and retrospectively mapped landslides from the years 1998 to 2017 across Taiwan.

2. Study area

Our study area is mainland Taiwan with an area of 35,874 km², located in the Western Pacific Ring of Fire, with frequent earthquakes and comprising 75% mountainous regions (Fig. 1). Despite a rugged terrain, it is densely populated with 610 people per km². Hilly terrain, earthquakes and precipitation are the main underlying drivers of landslides. Taiwan has an average annual precipitation of 2,500mm, varying between mountainous regions (max 4,800mm) and plains (min 1100mm) (Fig. 1). Due to its geographical positioning in a sub-tropical zone in the Pacific, Taiwan annually suffers from on-land tropical cyclone strikes (so-called typhoons) three-four times a year. Among the historical typhoons, disasters related to Typhoon Morakot (7 to 9 August 2009) produced an accumulated rainfall of 2,777 mm (Ge et al. 2010), landslides and debris flows, resulting in nearly 700 deaths and approximately 4.7 billion USD in damage.

3. Methods

The workflow entailed four steps to map landslide occurrence on an annual basis (Fig. 2). First, we extracted several remote sensing variables from Landsat time-series, DEM, and nighttime light data. We used cloud-free pixels and developed pixel-based composites of images (layerstacks) (Section 3.1). To adopt a supervised classification, we created training and validation sample sets from visually validated reference maps (Section 3.2). Second, to develop an accuracy-balanced random forest model, we conducted a sensitivity analysis of class ratios (the optimal ratio of training samples) (Section 3.3). We used layerstacks with different sets of inputs (seasonal features, nighttime light, and slope), statistically tested

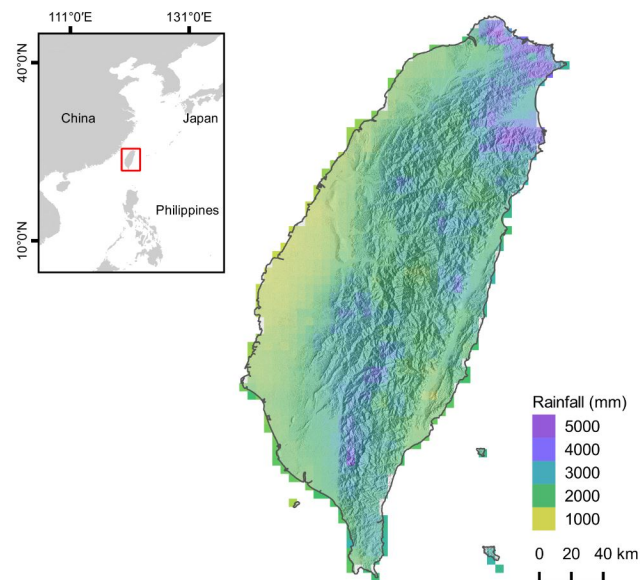


Figure 1: Map of Taiwan with hill shade and the average annual precipitation of 1963–2012. (Source of rainfall data: TCCIP).

our two hypotheses, and then selected the best model (Section 3.4). Thirdly, we validated with independent samples the applicability of the best model for other years with subsampled replicates (Section 3.5). Finally, we applied the RF model to map annual landslide occurrence explicitly from 1998 to 2017, demonstrating how these maps can be used to identify spatiotemporal patterns of landslide activities (Section 3.6).

3.1. Datasets

Three datasets were utilized to derive variables for landslide classification (Table 1): (1) seasonal spectral features, such as NDVI, were derived from Landsat multispectral images, (2) slope was derived from the Global Digital Elevation Model of the Advanced Spaceborne Thermal Emission and Reflection Radiometer (ASTER GDEM) and (3) nighttime light data were based on DMSP and VIIRS. The variables derived from these datasets are listed in Table 1. All the variables were resampled to 30m pixel size with the nearest neighbor method.

3.1.1. Landsat data

We downloaded from the USGS archive all available Level-2 Landsat-5, Landsat-7 and Landsat-8 imagery from

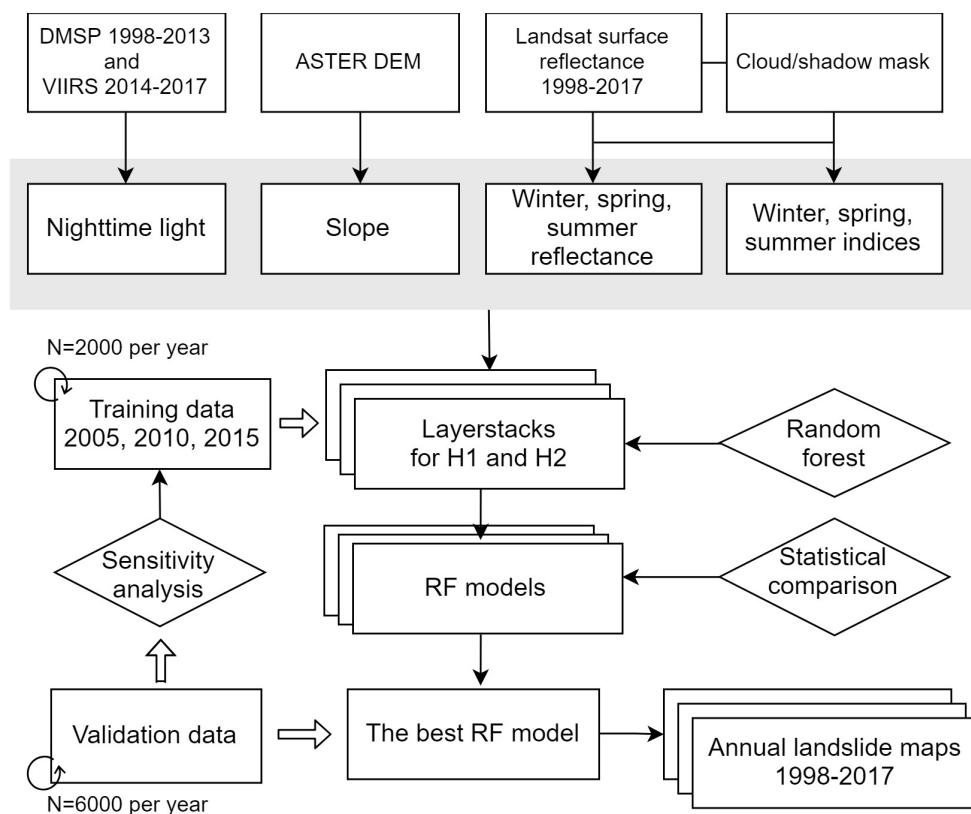


Figure 2: Flowchart of long-term landslide mapping based on open-access satellite datasets.

1998 to 2017 for the five Landsat tiles covering Taiwan (World Reference System WRS-2 path/row 117/43, 117/44, 117/45, 118/43, 118/44). Level-2 products are surface reflectance data at a 30m spatial resolution with systematic terrain correction and atmospheric correction, and are provided with per-pixel quality information, including a cloud mask produced with the CFMask algorithm (Foga et al. 2017). We used the quality band to remove middle- and high-confidence cloud pixels. Areas of gaps caused by the scan line corrector failure (known as SLC-off) of Landsat-7 ETM+ were not processed for surface reflectance (Markham et al. 2004). This step allowed us to avoid value anomalies but increased data loss, which was pronounced along the edge of the scenes, covering the middle part of our study area. We utilized the blue, green, red, near infrared, first and second shortwave infrared bands. NDVI and NDWI were first calculated for each single-date image (see formulas in Table 1). Then, the values of the bands and the indices were calculated as seasonal means in winter (December of the previous year to February), spring (March to May), and summer (June to August). This fusion step increased cloud-free observations (Fig. S1, Appendix A). We excluded images from September to November (Autumn), considering the fluctuation of typhoon perturbation and short-term vegetation recovery.

3.1.2. Aster GDEM data

The ASTER GDEM (obtained from <https://gdex.cr.usgs.gov/>) is a product of NASA and METI and was generated from ASTER imagery with a resolution of 30m. The elevation is assumed to be static in this study and we used the only single-time product of GDEM that is produced from stereo-pairs acquired from 2000 to 2011 to represent the general topography. Elevation information was used to derive the slope variable.

3.1.3. Nighttime light data

Nighttime light datasets include cloud-free DMSP data (1998-2013) and VIIRS data (2014-2017) and were downloaded from <https://www.ngdc.noaa.gov/eog/>. The DMSP annual composite data contain average radiance values of cloud-free coverages (Fig. S1, Appendix A), reflecting the persistent lights from cities, villages, and roads, with a spatial resolution of about 900m, and a temporal coverage of 1992 to 2013 (Elvidge et al. 2017; Imhoff et al. 1997). Starting in 2013, VIIRS data is available with a finer spatial resolution of 450m approximately. As this newer data are only available in monthly composites (in contrast to the DMSP data which were aggregated to annual data), we used March data, with less cloud cover (Fig. S1, Appendix A) and the least number of Taiwanese holidays reducing in and out-migration, thus ensuring relatively stable lighting. To make VIIRS data comparable with DMSP data, we

adopted a two-step procedure to spectrally stretch VIIRS data by the products in the overlapping year of 2013 for the study area. First, we removed outliers by forcing values greater than 40 and lower than 0.2 to 40 and 0.2, respectively. Second, we correlated the two datasets using a logarithmic transformation, producing a correlation coefficient of 0.94. We thus used a linear-log regression to stretch outlier-removed VIIRS data from 2014 to 2017 as follows:

$$V' = 26.139 \times \log_{10}(V) + 23.179$$

where V' is the stretched VIIRS data, 26.139 is the slope, V is the outlier-removed VIIRS data, and 23.179 is the intercept.

3.2. Training and validation data collection

To produce training and validation datasets, we used reference landslide maps (2005-2016) from the Taiwan Council of Agriculture (data available from <https://www.tgos.tw>, also presented in Fig. S3, Appendix A). The twelve annual landslide maps covering the whole area of Taiwan were created with semi-automatic image classification approach (multispectral Formosat-2 satellite images at 2m resolution were taken between January and July). Non-vegetated areas that are not landslides were manually corrected, including human land use, river sediments, and displaced materials (debris/rock) overlying along gentle slopes. The minimum size of detected landslide objects was 1,000 m². These reference maps were validated by visual interpretation of national aerial photos with 98% of overall accuracy (Lin et al. 2013).

Training and validation sample sets were produced for ‘landslide’ and ‘non-landslide’ classes. We created sample points with an account for spatial autocorrelation, as spatial autocorrelation of the sample may reduce the representativeness of sampling (Millard and Richardson 2015). We measured spatial autocorrelation with Moran’s I (Ord 2004) and found that the spatial autocorrelation rapidly decreased (from 0.9 to 0.7) between 0-3 pixels. Thus, we sampled points by keeping the minimum distance of 100m (> 3 pixels). Using this distance limit, the first sets of training and validation data were produced independently without overlap (validation points at the distance of 0-100 m from training sample were removed). The training set included 60,000 points for each of training years (2005, 2010, and 2015), and validation set included around 110,000 points for each of test years (2005-2016) (Table 2). The two sets were used for sub-sampling (drawing a small number of points) when classification and accuracy tests were iteratively implemented.

3.3. Sensitivity analysis

We noticed that the class distribution was unbalanced, thus potentially introducing a bias of classification with overestimation of the dominant (non-landslide) and

Table 2: Size of training and validation sets comprising points from different years. Points with missing values were removed. The two sample sets were used for iterative cross-validation.

Year	Training set		Validation set	
	Landslide	Non-landslide	Landslide	Non-landslide
2005	5961	49830	3901	105415
2006	-	-	4413	108185
2007	-	-	4409	112879
2008	-	-	4663	107630
2009	-	-	2836	111631
2010	13309	49758	8124	105846
2011	-	-	6396	103638
2012	-	-	6587	103198
2013	-	-	6195	108040
2014	-	-	6535	106919
2015	8676	49657	6505	111444
2016	-	-	4966	111576

underestimation of the rare class (landslide) (Dalponte et al. 2013). To evaluate the impact of unbalanced class distribution on the accuracy, we applied a sensitivity analysis approach proposed by Stumpf and Kerle 2011 that tests different class ratios (β) to define the optimal ratio of training samples to find an optimal balance between user’s (overestimation) accuracy and producer’s (underestimation) accuracy. For the analysis of class ratio optimization and the final classification and accuracy assessment, a 50-fold-iterative procedure was performed for each model. For each iteration, we adjusted the Stumpf and Kerle approach, by using a consistent total sample size to avoid a confounding sample size effect. In this way, 2000 training points for 2005, 2010, and 2015 were randomly drawn from the large training set, and 6000 validation points for each of the test years from the validation set were subsampled as test set (Fig. 2). The parameter β_i refers to the ratio of landslide and non-landslide samples in the training set and was changed iteratively to approach an optimal value β_n balancing producer’s and user’s accuracies. The procedure started from an equal class distribution ($\beta_i = 1$), which defines the sample size for landslide ($2000/(1 + \beta_i)$) and non-landslide ($2000 \times \beta_i/(1 + \beta_i)$), and in each step β_i was increased by 0.1 until reaching a non-landslide-fivefold class distribution ($\beta_i = 5$). To help the classifier to better learn the complexity of non-landslide activities, we ensured a minimum number of points (N=100) for six non-landslide land covers (building, road, agriculture, forest, non-landslide barren land, and water). In each iteration, 100 points were first allocated to every land cover class and then the remaining points were proportionally allocated.

3.4. Classification methods

To map landslides, we used Random Forest (RF), a non-parametric machine learning classifier that has proven to accurately differentiate spectrally complex classes (Belgiu and Drăguț 2016). A RF classifier is an ensemble classifier that grows multiple decision trees and are trained using bagging, thereby letting the trees determine the

probability of the class membership. RF performs multiple criteria classification, being at the same time fast and insensitive to overfitting (Breiman 2001). We utilized a version of RF implemented in the R statistical software with the randomForest package (Liaw and Wiener 2002).

RFs were trained with a combined training data subset from 2005, 2010, and 2015, which was class-ratio-adjusted. For parameterizing the RF classifier, based on out-of-bag accuracy, we used 500 trees and took the square root of the number of layers as a split criterion at each node. We ran two classification scenarios (Table 3) to test the two hypotheses that multi-seasonal imagery (H1) and nighttime light (H2) results in higher classification accuracy. To test H1, we classified a layerstack including bands and indices from three seasons (winter, spring and summer) and compared with the classification outcomes when only one single season was used. To test H2, we classified a layerstack with and without the additional inclusion of nighttime light data. We first separately estimated the optimal class ratio (β) for the H1 and H2 models by 50 iterations for each model with randomly subsampled training and validation datasets (with replacement). Based on their optimal numbers, we assessed the accuracies and statistically compared producer’s and user’s accuracies of the models for H1 and H2 using t-test at $\alpha=0.001$.

3.5. Accuracy assessment

To test whether the final model trained with the β_n -adjusted sample from the three years (2005, 2010 and 2015) is robust and applicable to other years, we used validation samples from twelve years (2005-2016) to evaluate annual accuracies. Although a random forest classifier calculates out-of-bag cross-validation accuracy, we relied on independent validation datasets for the final accuracy assessment. We subsampled 6,000 points for each of the tested years. Since the equal allocation of validation samples for unbalanced classes is not appropriate for area estimation and proportional allocation may result in imprecise estimates of user’s accuracy for the rare class (a landslide in our case), we adopted an alternative sample allocation approach proposed by Olofsson et al. 2014. We examined the standard errors of the estimated user’s accuracy and the estimated area and allocated 500 points for a landslide, and the remaining 5500 points were allocated to the non-landslide class.

These points were evaluated as one of four validation categories: true positive (TP), true negative (TN), false negative (FN), false positive (FP). TPs represent spatially and temporally correct landslide points, TNs are correct non-landslide points, FNs are reference landslide points

missing in the detection and FPs are points identified as landslide but are not present in the reference map. Based on these categories, we calculated overall accuracy $((TP + TN) / (TP + TN + FP + FN))$, user’s accuracy $(TP / (TP + FP))$, and producer’s accuracy $(TP / (TP + FN))$. The user’s accuracy represents the model performance in reducing landslide overestimation and producer’s accuracy refers to the ability to minimize landslide underestimation. We implemented 100 subsampled replications to estimate the mean and standard deviation for the overall accuracy, user’s accuracy and producer’s accuracy for each test year.

3.6. Deriving spatiotemporal patterns of landslide activities

Based on the best RF model (Section 3.4) we derived the annual landslide / non-landslide maps from 1998 to 2017. To characterize the different types of long-term risk of landslides, we calculated the frequency, first occurrence, persistence and reoccurrence landslide metrics from the derived maps. First occurrence is the year the landslide was first observed from 1998 to 2017. Persistence expresses the longest number of consecutive years of landslide occurrence at a location. The frequency metric is a landslide rate (occurrences from 1998 to 2017 divided by the number of years). The reoccurrence metric addresses the number of landslide intervals. An interval ended if a pixel experienced revegetation (becoming non-landslide) in a year after landslide occurrence.

4. Results

We present our results in four parts: the sensitivity analysis (Section 4.1) and model comparison (Section 4.2), which suggested that multi-seasonal imagery and nighttime light resulted in statistically significantly more accurate classification accuracies ($p < 0.001$). When those features were used, the validation of the final model showed that user’s and producer’s accuracies over test years ranged from 73% to 86% (Section 4.3). In last Section 4.4, the application results of detecting spatiotemporal patterns with the developed model were obtained.

4.1. Sensitivity analysis

For all six models, we observed a strong over-estimation of landslide areas if samples of the two classes were equally sized ($\beta = 1$) (Fig. 3). The over-estimation of landslide areas was even more pronounced if single-season models were utilized. By iteratively increasing β_i the balance of user’s and producer’s accuracies was found to vary

Table 3: Variables used for hypothesis 1 and 2.

Classification scenario	Target layerstack	Compared layerstack
(H1) Multiple seasonal imageries	Bands, indices in winter, spring, summer and slope	Bands, indices in a single season and slope
(H2) Nighttime light data	Bands, indices in winter, spring, summer, slope and nighttime light	Bands, indices in winter, spring, summer and slope

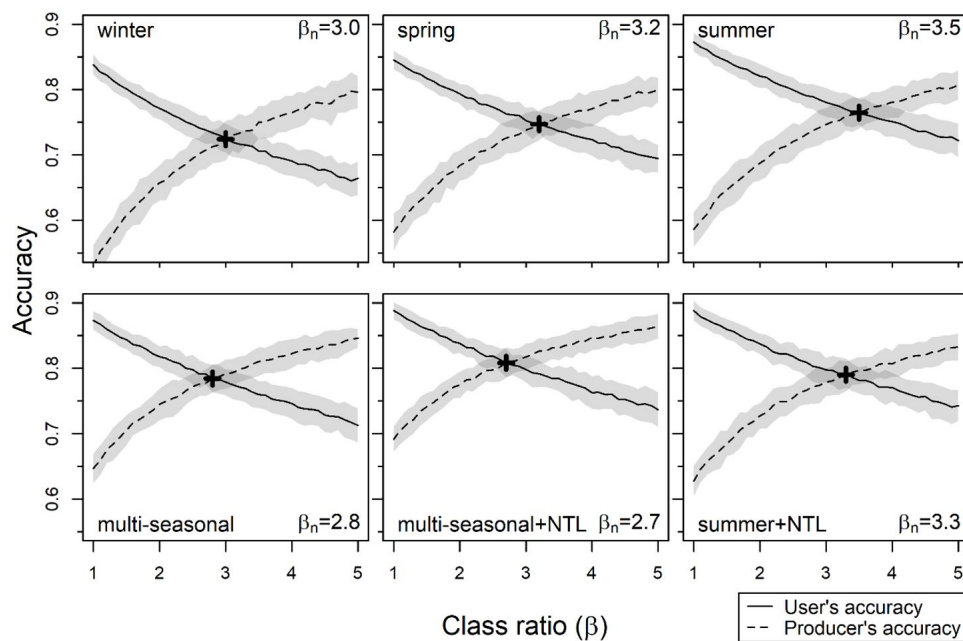


Figure 3: Estimates of the optimal class ratio (β_n) that achieves a balance between user's accuracy (solid line) and producer's accuracy (dot line). The lines indicating the mean of the accuracy were produced from 50-fold subsampling runs for each β_i . The grey margins show 95% confidence intervals.

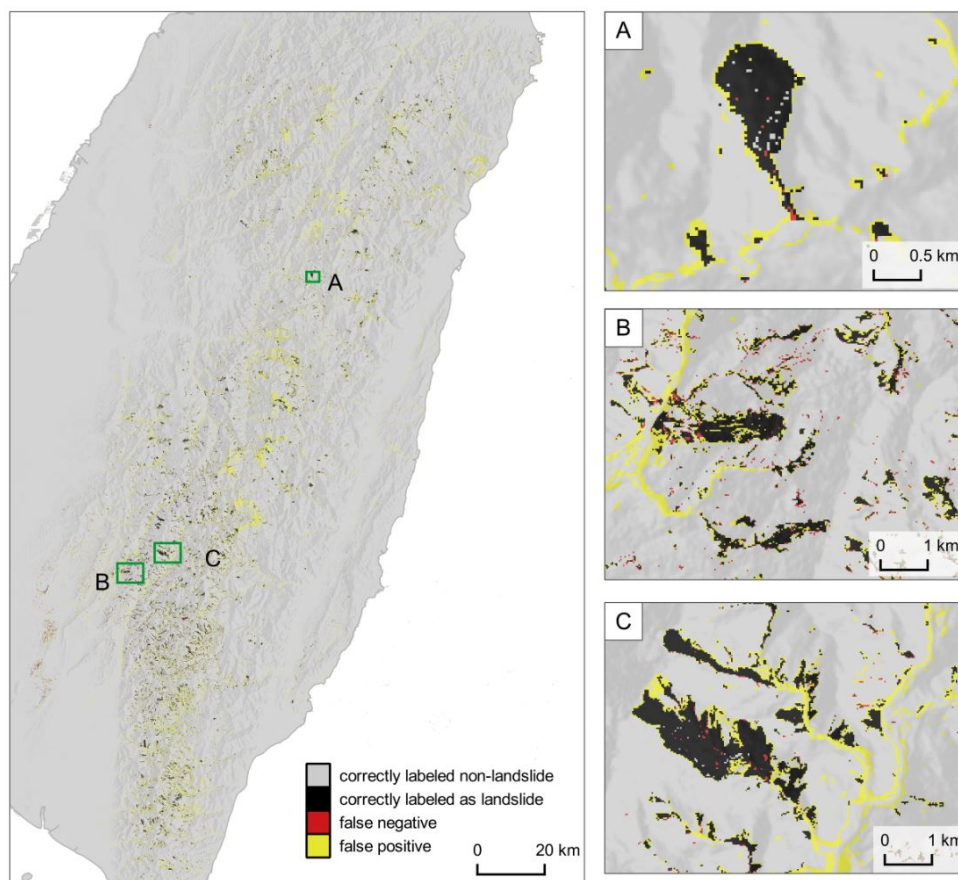


Figure 4: Final map based on the best model (classified multi-seasonal imagery combined with nighttime light data) for the year 2011, in comparison with a reference map. A: landslides on north-south slopes. B: a deep-seated landslide occurred at a village during the typhoon Morakot. C: large-scale landslides. False positives (yellow) from the displaced rock and debris retained as they were classified without manual elimination.

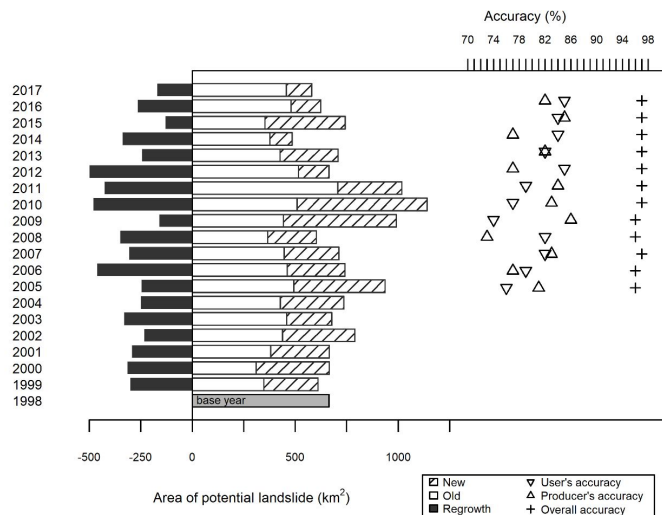


Figure 5: Estimated landslide area split into old landslide area (year t-1 and year t: landslide), new landslide area (year t-1: non-landslide and year t: landslide), and revegetated area (year t-1: landslide and year t: non-landslide), with user’s accuracies, producer’s accuracies, and overall accuracies from validated maps 2005–2016. The area (km²) is adjusted for missing areas from clouds and SLC-off gaps.

from 2.7 to 3.5 across the six models (Fig. 3). Since the optimal class ratio was model-dependent, we used the optimal ratio for each model independently for further model comparisons.

4.2. Effects of using nighttime lights and multi-seasonal imagery

Results of the t-test for scenario (H1) (Table 4) show that the multi-season model that includes the variables from all three seasons achieved balanced user’s and producer’s accuracies of 78%, and performed statistically significantly more accurate ($p < 0.001$) compared to single-season models for winter, spring and summer. Among the single-season models, summer and spring yielded statistically more accurate classification accuracies (user’s and producer’s accuracies range of 74–76%) than the winter model, with user’s and producer’s accuracy around 72%. For scenario (H2) (Table 5), combined nighttime light data and multi-seasonal satellite imagery resulted in a statistically more accurate classification accuracy (balanced user’s accuracy and producer’s accuracy of 81%), compared to classified multi-seasonal satellite imagery alone (of 78%). In the best model, nighttime light and slope have higher importance than other variables (Fig. S2, Appendix A).

4.3. Transferability of the model over time

When applying the best model, including variables of nighttime light, slope, and multiple seasonal bands, NDVI, and NDWI, our accuracy assessment results showed that the overall accuracies in other years ranged from 96% to 97% (Table 6). The user’s accuracies varied between 74 and 85% and producer’s accuracies were between 73 and

86%, implying that the model can be applied also for other years. We observed that user’s accuracy in years 2014 to 2016 were higher (average of 84%) than previous years (average of 80%) (Table 6), indicating that the higher resolution of nighttime light data helps to reduce over-prediction.

The validated landslide map for 2011 showed the landslides at different locations, their sizes, and shapes (Fig. 4). Landslides dominated in the middle and southern parts of the central mountain range. A subset (Fig. 4A) illustrates how landslides were better depicted when landslide geometry was more compact. Although the compact and massive landslides were successfully detected, false positives were predominantly distributed along the edge of the small landslides, where mixed pixels are common. Inset (Fig. 4B) highlights the classified occurrence of a disastrous deep-seated landslide induced by extreme rainfall on 8 August 2010 – the “Shiaolin landslide” that destroyed a village, causing 491 fatalities. Deep-seated landslides are usually larger than shallow landslides. Fig. 4C presents a large-scale landslide at the vicinity of Fig. 4B.

We identified the composition of existing landslides, which we classified into old ones, new ones, and also revegetated areas (Fig. 5). After the dramatic Chi-Chi earthquake in late 1999, the overall landslide area in 2000 was only 6% higher compared to that prior to the earthquake. However, the estimate of new landslide areas indicated a significant increase by 34% compared to the previous year, which shows how extreme this event was.

4.4. Characterizing spatiotemporal patterns of landslide activities

We applied the most accurate model (incorporating variables of nighttime light, slope, and multiple seasonal bands, NDVI, and NDWI) for annual mapping landslides from 1998 to 2017 across Taiwan. The results showed that landslide areas varied from 1998 to 2017 across Taiwan (Fig. 5) with an increase in landslide occurrence in the south of Taiwan (Fig. 6).

The landslides in the northern regions were mostly triggered before 2002 and after the Chi-Chi earthquake in 1999 (Fig. 6), while landslides in the southern regions predominantly occurred from 2009, corresponding to the timing of typhoon Morakot. The temporal patterns of landslide activities are different between a northern site (Fig. 6A) and a southern site (Fig. 6B), in terms of frequency, persistence, and reoccurrence.

5. Discussion

We developed an approach using freely available Landsat multi-seasonal imagery and nighttime light data to reconstruct long-term dynamics of landslides in Taiwan. Event-based commercial very high-resolution landslide maps are usually used for depicting morphological changes

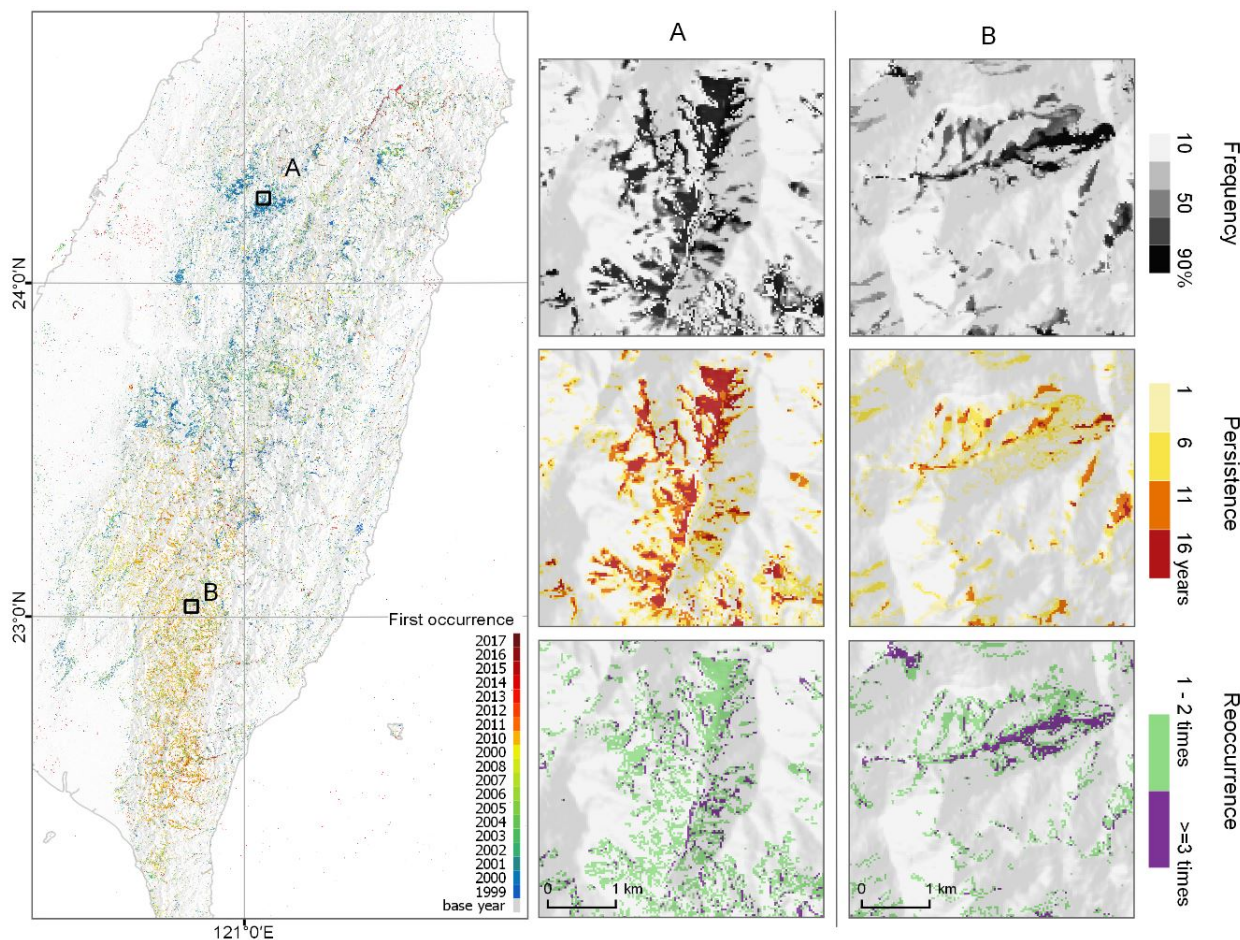


Figure 6: First occurrence of landslides from 1998 to 2017. (A) An earlier occurring area and (B) a post-Morakot landslide area. Both sites present high frequency, while (A) is of high persistence, and (B) is of high reoccurrence.

in size, length, and symmetry of the individual landslides. Yet, freely available medium resolution Landsat imagery and nighttime light data allows the long-term and large-scale assessment of landslide patterns, thus providing knowledge about frequency, persistence, and reoccurrence

of landslide activities. Our study underscored the utility of the synergetic use of nighttime light data and multi-seasonal imagery to map landslides annually. With the metrics including multiple seasonal bands, NDVI, NDWI, slope, and nighttime light, the RF classifier

Table 4: Statistical comparison of the models to test Hypothesis 1 (multi-seasonal imagery versus single-season imagery). Mean of accuracies for each case was estimated by runs of subsampling and based on identification of the optimal class ratio (β). T-tests were run to test whether the mean of accuracies for each model was statistically more accurate compared to the base model (winter).

Model	β_n	Overall accuracy	User's			Producer's		
			accuracy	t value	p-value	accuracy	t value	p-value
Winter	3.0	95.4%	72.2%	—	—	72.6%	—	—
Spring	3.2	95.8%	74.5%	8.5	<0.001	74.9%	11.6	<0.001
Summer	3.5	96.1%	76.4%	15.1	<0.001	76.6%	18.3	<0.001
Multiple seasons	2.8	96.4%	78.5%	23.2	<0.001	78.4%	26.1	<0.001

Table 5: Statistical comparison of the models to test Hypothesis 2. T-tests were run to test whether the mean of accuracies of multi-seasonal imagery combined with nighttime light data was statistically more accurate compared to classified multi-seasonal imagery alone.

Model	β_n	Overall accuracy	User's			Producer's		
			accuracy	t value	p-value	accuracy	t value	p-value
Non-nighttime light (multiple seasons)	2.8	96.4%	78.5%	—	—	78.4%	—	—
Nighttime light (multiple seasons)	2.7	96.8%	80.8%	10.5	<0.001	80.8%	10.8	<0.001

Table 6: Annual overall, user’s and producer’s accuracies (%) based on different nighttime light (NTL) resolution. The mean values and 95% confidence intervals (\pm) were estimated from 100 iterations with subsampling of 6000 samples.

Year	Overall accuracy	UA	PA	NTL resolution
2005	96 \pm 1	76 \pm 4	81 \pm 4	
2006	96 \pm 1	79 \pm 3	77 \pm 4	
2007	97 \pm 1	82 \pm 3	83 \pm 4	
2008	96 \pm 1	82 \pm 3	73 \pm 4	
2009	96 \pm 1	74 \pm 3	86 \pm 3	900m
2010	97 \pm 1	77 \pm 3	83 \pm 4	
2011	97 \pm 1	79 \pm 3	84 \pm 4	
2012	97 \pm 1	85 \pm 4	77 \pm 4	
2013	97 \pm 1	82 \pm 3	82 \pm 4	
2014	97 \pm 1	84 \pm 3	77 \pm 4	
2015	97 \pm 1	84 \pm 3	85 \pm 3	450m
2016	97 \pm 1	85 \pm 3	82 \pm 4	

reached an overall accuracy of 97%, and a balanced user’s and producer’s accuracies of 81%. When applying the developed RF model for other years without training samples for the respective years, we also achieved high overall, user’s, and producer’s accuracies (96-97%, 74-85%, and 73-86%). The accuracies achieved are more balanced compared to other recent studies of large-scale landslide detection in Asia, with user’s and producer’s accuracy at 58% and 87% based on a multi-sensor approach (resolution at 5m-30m) for long-term landslide mapping (Behling et al. 2016), and at 32% and 63% based on single-temporal Landsat imagery (Yu and Chen 2017). Our approach is comparable in accuracy to a study on landslide detection based on object-based classification of optical imagery and DEM at higher resolution (2-10m) which also reaches balanced accuracies between 73% and 87% (Stumpf and Kerle 2011).

We found nighttime light imagery helpful for increasing classification accuracy of landslides in anthropogenic areas. Despite its relative coarse resolution, luminosity from built-up areas and road lights allows the models to account for the human activities not affected by landslides and thus to separate them from landslide affected areas. Earlier studies have found the usefulness of nighttime light imagery to assess the changes in population density, various economic activities and technological shifts (Bennett and Smith 2017; Rybnikova and Portnov 2017). To our knowledge, the current study is the first to test the suitability of employing nighttime light imagery to study landslides. Our results suggest that the use of nighttime light data helps in disentangling the complex interrelationship between spectral signatures of natural and human-managed land cover classes, and therefore is of usefulness in mapping impacts of hazards.

We found that for highly populated Taiwan multi-seasonal imagery resulted in more accurate classification of landslides than single-season imagery. The use of machine-learning random forest is powerful in separating multi-dimensional seasonal signals. For instance, built-up areas have stable reflectance across

winter, spring and summer, while landslides may have fluctuating reflectance values across the year due to the contribution from the varying vegetation signals associated with regrowth. Several studies have proven the utility of multi-seasonal imagery and multiple criteria classifiers to accurately classify various land-cover types and land use (Oetter et al. 2001; Guerschman et al. 2003; Bleyhl et al. 2017; Gao et al. 2015; Grădinaru et al. 2017). Our study highlights the power of multi-seasonal imagery for accurately mapping landslides.

Landslides are widespread throughout the world but tend to have been mapped in details and only at a very localized scale or for a short duration (Van Westen et al. 2006). The current global database of landslides records only fatal landslides (Petley 2012), and is not updated with past landslides and whether areas of landslides were recovered or rehabilitated. Taiwan has a very dynamic landslide environment, driven by high precipitation events, frequent earthquakes, and fast vegetation regrowth (Chang et al. 2007). We found an inter-annual fluctuation of the total potential landslide area between 478 to 1130 km² in Taiwan without a consistent increase or decrease between 1998 and 2017. This absence of a trend is in contrast to the continuing upward trend of globally recorded landslides (Petley 2012). We observed that landslide areas could largely recover within a year (Fig. 5), and that landslide areas decreased by 35% from 2011 to 2012 and by 32% from 2013 to 2014. In contrast, the highest growth rate from 2008 to 2009 (65%), is explained by the tropical cyclone Morakot that hit Taiwan in August 2009, confirming the general trend observed by Petley 2010 that the major driver of landslides in East Asia is tropical cyclones.

There were some limitations in our study, such as a necessity to fuse multi-sensor imagery. Multi-sensor images may have different spatial, spectral, temporal and radiometric resolutions (Pohl and Van Genderen 1998) and for instance an intercalibration of DMSP and VIIRS nighttime light data is required. To mitigate the impacts of application of inconsistent data, we trained our model by selecting training years covering different sensors’ span. Additionally, nighttime light data have a relatively coarse resolution (at best 500m) which differed from the 30-m Landsat imagery we utilized in our study. Nevertheless, a combination of multi-sensor data allows increasing the time span of observations, and facilitates highlighting specific phenomena, which may not be possible to detect with a single remote sensing product (e.g., optical imagery).

Our landslide maps did not fully cover our study area, because of data availability of optical imagery in this cloud-prone region. Therefore, we missed detection of landslides in Taiwan for 13% and 11% of the total area in 1998 and 2013, respectively, as there were less accessible images (before Landsat-7 launched in 1999 and right after Landsat-5 stopped collecting data in 2013). Where image availability and cloud-contamination is an

issue, the number of observations can be complemented with additional use of radar (e.g., Sentinel-1 since 2013) imagery, as well as fusion using images from MODIS and Landsat (Zhu et al. 2016). We did not test the performance of higher resolution remotely sensed products that are also freely available, such as from the Sentinel-2 MSI time-series imagery. Sentinel-2 MSI imagery has high potential to enhance classification of landslides with higher spatial accuracy, but limited historical coverage. What our study showed is that, even with radiometrically coarse DMSP nighttime light data and optical Landsat imagery, it is possible to reconstruct historical landslides as early as the early 1990s accurately.

Despite some limitations, we propose the idea of using cost-effective data and methods to provide knowledge of historical landslide inventories, reflecting landslide first occurrence, persistence, as well as identify reoccurring landslide activities. Compared to areas showing only recent landslides, the areas of persistent landslides are more predictable and land-use plans around these regions can be formulated in advance. The reoccurrence rate is related to the depths of the sliding plane, which is useful for identifying remediation strategies. These annual landslide maps also provide a basis for studies on drivers of landscape changes and to help develop policy interventions.

6. Conclusions

Here we explored the effectiveness of nighttime light and multi-seasonal imagery to provide improved landslide image classification and for the derivation of long-term landslide maps in Taiwan from 1998 to 2017. Our findings confirmed that nighttime light and multi-seasonal optical imagery could significantly improve landslide mapping accuracies. This approach proved to be robust and transferable to historical mapping of landslides over a long period (20 years). We demonstrate the usefulness of long-term landslide maps that allow characterizing spatio-temporal patterns of landslide characteristics such as first time of occurrence, persistence and reoccurrence rate. Notably, during the period 1998 to 2017 the patterns of high landslide occurrence shifted from the north to the south of Taiwan. Our findings of the utility of nighttime light imagery and optical multi-seasonal imagery to map retrospective landslides can likely be replicated elsewhere, particularly because of the growing archives of freely available optical Landsat-like multi-seasonal imagery and refined VIIRS nighttime light data.

Acknowledgement

This work was supported by a Ph.D. scholarship from the Ministry of Education, Taiwan, and by BERTHA - the Danish Big Data Centre for Environment and Health funded by the Novo Nordisk Foundation Challenge

Programme (grant NNF17OC0027864). The authors wish to thank the three anonymous reviewers for very thorough and constructive reviews, and Tzu-Yin Kasha Chen for comments on geomorphological explanation.

References

- Althuwaynee, Omar F, Biswajeet Pradhan, and Saro Lee (2012). "Application of an evidential belief function model in landslide susceptibility mapping". In: *Computers & Geosciences* 44, pp. 120–135.
- Barlow, J, Y Martin, and SE Franklin (2003). "Detecting translational landslide scars using segmentation of Landsat ETM+ and DEM data in the northern Cascade Mountains, British Columbia". In: *Canadian journal of remote sensing* 29.4, pp. 510–517.
- Behling, Robert, Sigrid Roessner, Darya Golovko, and Birgit Kleinschmit (2016). "Derivation of long-term spatiotemporal landslide activity—A multi-sensor time series approach". In: *Remote Sensing of Environment* 186, pp. 88–104.
- Behling, Robert, Sigrid Roessner, Hermann Kaufmann, and Birgit Kleinschmit (2014). "Automated spatiotemporal landslide mapping over large areas using rapideye time series data". In: *Remote Sensing* 6.9, pp. 8026–8055.
- Belgiu, Mariana and Lucian Drăguț (2016). "Random forest in remote sensing: A review of applications and future directions". In: *ISPRS Journal of Photogrammetry and Remote Sensing* 114, pp. 24–31.
- Bennett, Mia M and Laurence C Smith (2017). "Advances in using multitemporal night-time lights satellite imagery to detect, estimate, and monitor socioeconomic dynamics". In: *Remote Sensing of Environment* 192, pp. 176–197.
- Bleyhl, Benjamin et al. (2017). "Assessing landscape connectivity for large mammals in the Caucasus using Landsat 8 seasonal image composites". In: *Remote Sensing of Environment* 193, pp. 193–203.
- Borghuis, AM, K Chang, and HY Lee (2007). "Comparison between automated and manual mapping of typhoon-triggered landslides from SPOT-5 imagery". In: *International Journal of Remote Sensing* 28.8, pp. 1843–1856.
- Breiman, Leo (2001). "Random forests". In: *Machine learning* 45.1, pp. 5–32.
- Chang, Kang-Tsung, Shou-Hao Chiang, and Mei-Ling Hsu (2007). "Modeling typhoon-and earthquake-induced landslides in a mountainous watershed using logistic regression". In: *Geomorphology* 89.3-4, pp. 335–347.
- Chen, Sheng-Chuan, Chia-Chi Chang, Hsun-Chuan Chan, Long-Ming Huang, and Li-Ling Lin (2013). "Modeling typhoon event-induced landslides using GIS-based logistic regression: a case study of Alishan forestry railway, Taiwan". In: *Mathematical Problems in Engineering* 2013.

- Chen, Tzu-Hsin and Kuan-Hui Elaine Lin (2018). “Distinguishing the windthrow and hydrogeological effects of typhoon impact on agricultural lands: an integrative OBIA and PPGIS approach”. In: *International journal of remote sensing* 39.1, pp. 131–148.
- Chigira, Masahiro, Xiyong Wu, Takashi Inokuchi, and Gonghui Wang (2010). “Landslides induced by the 2008 Wenchuan earthquake, Sichuan, China”. In: *Geomorphology* 118.3-4, pp. 225–238.
- Chuang, Yung-Chung and Yi-Shiang Shiu (2018). “Relationship between landslides and mountain development—Integrating geospatial statistics and a new long-term database”. In: *Science of the Total Environment* 622, pp. 1265–1276.
- Dalponte, Michele, Hans Ole Orka, Terje Gobakken, Damiano Gianelle, and Erik Næsset (2013). “Tree species classification in boreal forests with hyperspectral data”. In: *IEEE Transactions on Geoscience and Remote Sensing* 51.5, pp. 2632–2645.
- Database, The Emergency Events (2018). *The Emergency Events Database - Université catholique de Louvain (UCL) - CRED, D. Guha-Sapir, Brussels, Belgium.* <https://www.emdat.be>.
- Doll, Christopher NH, Jan-Peter Muller, and Jeremy G Morley (2006). “Mapping regional economic activity from night-time light satellite imagery”. In: *Ecological Economics* 57.1, pp. 75–92.
- Dong, Jie et al. (2018). “Mapping landslide surface displacements with time series SAR interferometry by combining persistent and distributed scatterers: A case study of Jiaju landslide in Danba, China”. In: *Remote sensing of environment* 205, pp. 180–198.
- Elvidge, Christopher D, Kimberly Baugh, Mikhail Zhizhin, Feng Chi Hsu, and Tilottama Ghosh (2017). “VIIRS night-time lights”. In: *International Journal of Remote Sensing* 38.21, pp. 5860–5879.
- Fell, Robin et al. (2008). “Guidelines for landslide susceptibility, hazard and risk zoning for land use planning”. In: *Engineering Geology* 102.3, pp. 85–98.
- Foga, Steve et al. (2017). “Cloud detection algorithm comparison and validation for operational Landsat data products”. In: *Remote sensing of environment* 194, pp. 379–390.
- Gao, Tian et al. (2015). “Mapping spatial distribution of larch plantations from multi-seasonal Landsat-8 OLI imagery and multi-scale textures using random forests”. In: *Remote Sensing* 7.2, pp. 1702–1720.
- Ge, Xuyang, Tim Li, Shengjun Zhang, and Melinda Peng (2010). “What causes the extremely heavy rainfall in Taiwan during Typhoon Morakot (2009)?” In: *Atmospheric science letters* 11.1, pp. 46–50.
- Golovko, Darya, Sigrid Roessner, Robert Behling, and Birgit Kleinschmit (2017). “Automated derivation and spatio-temporal analysis of landslide properties in southern Kyrgyzstan”. In: *Natural Hazards* 85.3, pp. 1461–1488.
- Grădinaru, Simona R, Felix Kienast, and Achilleas Psomas (2017). “Using multi-seasonal Landsat imagery for rapid identification of abandoned land in areas affected by urban sprawl”. In: *Ecological Indicators*.
- Guerschman, J Paruelo, JM Paruelo, C Di Bella, MC Giallorenzi, and F Pacin (2003). “Land cover classification in the Argentine Pampas using multi-temporal Landsat TM data”. In: *International Journal of Remote Sensing* 24.17, pp. 3381–3402.
- Hervás, Javier et al. (2003). “Monitoring landslides from optical remotely sensed imagery: the case history of Tessina landslide, Italy”. In: *Geomorphology* 54.1-2, pp. 63–75.
- Hölbling, Daniel, Barbara Friedl, and Clemens Eisank (2015). “An object-based approach for semi-automated landslide change detection and attribution of changes to landslide classes in northern Taiwan”. In: *Earth Science Informatics* 8.2, pp. 327–335.
- Hong, Haoyuan et al. (2016). “Spatial prediction of landslide hazard at the Luxi area (China) using support vector machines”. In: *Environmental Earth Sciences* 75.1, p. 40.
- Hooper, Andrew, David Bekaert, Karsten Spaans, and Mahmut Arıkan (2012). “Recent advances in SAR interferometry time series analysis for measuring crustal deformation”. In: *Tectonophysics* 514, pp. 1–13.
- Imhoff, Marc L, William T Lawrence, David C Stutzer, and Christopher D Elvidge (1997). “A technique for using composite DMSP/OLS “city lights” satellite data to map urban area”. In: *Remote Sensing of Environment* 61.3, pp. 361–370.
- Jean, Neal et al. (2016). “Combining satellite imagery and machine learning to predict poverty”. In: *Science* 353.6301, pp. 790–794.
- Kennedy, Robert E, Zhiqiang Yang, and Warren B Cohen (2010). “Detecting trends in forest disturbance and recovery using yearly Landsat time series: 1. LandTrendr—Temporal segmentation algorithms”. In: *Remote Sensing of Environment* 114.12, pp. 2897–2910.
- Keyport, Ren N, Thomas Oommen, Tapas R Martha, KS Sajinkumar, and John S Gierke (2018). “A comparative analysis of pixel-and object-based detection of landslides from very high-resolution images”. In: *International journal of applied earth observation and geoinformation* 64, pp. 1–11.
- Khatami, Reza, Giorgos Mountrakis, and Stephen V Stehman (2016). “A meta-analysis of remote sensing research on supervised pixel-based land-cover image classification processes: General guidelines for practitioners and future research”. In: *Remote Sensing of Environment* 177, pp. 89–100.
- Li, Xianju, Xinwen Cheng, Weitao Chen, Gang Chen, and Shengwei Liu (2015). “Identification of forested landslides using LiDAR data, object-based image analysis, and machine learning algorithms”. In: *Remote sensing* 7.8, pp. 9705–9726.

- Liaw, Andy and Matthew Wiener (2002). "Classification and regression by randomForest". In: *R news* 2.3, pp. 18–22.
- Lin, EJ, CC Liu, CH Chang, IF Cheng, and MH Ko (2013). "Using the formosat-2 high spatial and temporal resolution multispectral image for analysis and interpretation landslide disasters in taiwan". In: *J. Photogramm. Remote Sens* 17.1, pp. 31–51.
- Makhamreh, Zeyad (2018). "Derivation of vegetation density and land-use type pattern in mountain regions of Jordan using multi-seasonal SPOT images". In: *Environmental Earth Sciences* 77.10, p. 384.
- Markham, Brian L, James C Storey, Darrel L Williams, and James R Irons (2004). "Landsat sensor performance: history and current status". In: *IEEE Transactions on Geoscience and Remote Sensing* 42.12, pp. 2691–2694.
- Martha, Tapas R, Norman Kerle, Cees J Van Westen, Victor Jetten, and K Vinod Kumar (2012). "Object-oriented analysis of multi-temporal panchromatic images for creation of historical landslide inventories". In: *ISPRS journal of photogrammetry and remote sensing* 67, pp. 105–119.
- Martha, Tapas Ranjan, Norman Kerle, Cees J van Westen, Victor Jetten, and K Vinod Kumar (2011). "Segment optimization and data-driven thresholding for knowledge-based landslide detection by object-based image analysis". In: *IEEE Transactions on Geoscience and Remote Sensing* 49.12, pp. 4928–4943.
- Martha, Tapas R et al. (2015). "Landslides triggered by the June 2013 extreme rainfall event in parts of Uttarakhand state, India". In: *Landslides* 12.1, pp. 135–146.
- Millard, Koreen and Murray Richardson (2015). "On the importance of training data sample selection in random forest image classification: A case study in peatland ecosystem mapping". In: *Remote sensing* 7.7, pp. 8489–8515.
- Nichol, J and MS Wong (2005). "Satellite remote sensing for detailed landslide inventories using change detection and image fusion". In: *International journal of remote sensing* 26.9, pp. 1913–1926.
- Oetter, Doug R, Warren B Cohen, Mercedes Berterretche, Thomas K Maiersperger, and Robert E Kennedy (2001). "Land cover mapping in an agricultural setting using multiseasonal Thematic Mapper data". In: *Remote Sensing of Environment* 76.2, pp. 139–155.
- Olofsson, Pontus et al. (2014). "Good practices for estimating area and assessing accuracy of land change". In: *Remote Sensing of Environment* 148, pp. 42–57.
- Ord, John K (2004). "Spatial processes". In: *Encyclopedia of Statistical Sciences* 12.
- Petley, David (2012). "Global patterns of loss of life from landslides". In: *Geology* 40.10, pp. 927–930.
- Petley, DN (2010). "On the impact of climate change and population growth on the occurrence of fatal landslides in South, East and SE Asia". In: *Quarterly Journal of Engineering Geology and Hydrogeology* 43.4, pp. 487–496.
- Pham, Mai Quyen, Pascal Lacroix, and Marie Pierre Doin (2018). "Sparsity optimization method for slow-moving landslides detection in satellite image time-series". In: *IEEE Transactions on Geoscience and Remote Sensing* 57.4, pp. 2133–2144.
- Pohl, Cle and John L Van Genderen (1998). "Review article multisensor image fusion in remote sensing: concepts, methods and applications". In: *International journal of remote sensing* 19.5, pp. 823–854.
- Pradhan, Biswajeet, Mustafa Neamah Jebur, Helmi Zuhaidi Mohd Shafri, and Mahyat Shafapour Tehrany (2016). "Data fusion technique using wavelet transform and Taguchi methods for automatic landslide detection from airborne laser scanning data and quickbird satellite imagery". In: *IEEE Transactions on Geoscience and remote sensing* 54.3, pp. 1610–1622.
- Prishchepov, Alexander V, Volker C Radeloff, Maxim Dubinin, and Camilo Alcantara (2012). "The effect of Landsat ETM/ETM+ image acquisition dates on the detection of agricultural land abandonment in Eastern Europe". In: *Remote Sensing of Environment* 126, pp. 195–209.
- Rau, Jiann-Yeou, Liang-Chien Chen, Jin-King Liu, and Tong-Hsiung Wu (2007). "Dynamics monitoring and disaster assessment for watershed management using time-series satellite images". In: *IEEE transactions on geoscience and remote sensing* 45.6, pp. 1641–1649.
- Rybnikova, Nataliya A and Boris A Portnov (2017). "Remote identification of research and educational activities using spectral properties of nighttime light". In: *ISPRS Journal of Photogrammetry and Remote Sensing* 128, pp. 212–222.
- Schneider, A et al. (2015). "A new urban landscape in East–Southeast Asia, 2000–2010". In: *Environmental Research Letters* 10.3, p. 034002.
- Sharma, Ram C, Ryutaro Tateishi, Keitarou Hara, Saeid Gharechelou, and Kotaro Iizuka (2016). "Global mapping of urban built-up areas of year 2014 by combining MODIS multispectral data with VIIRS nighttime light data". In: *International Journal of Digital Earth* 9.10, pp. 1004–1020.
- Singh, Krishna Kant and Akansha Singh (2016). "Detection of 2011 Sikkim earthquake-induced landslides using neuro-fuzzy classifier and digital elevation model". In: *Natural Hazards* 83.2, pp. 1027–1044.
- Stumpf, André and Norman Kerle (2011). "Object-oriented mapping of landslides using Random Forests". In: *Remote sensing of environment* 115.10, pp. 2564–2577.
- Stumpf, André, Jean-Philippe Malet, and Christophe Delacourt (2017). "Correlation of satellite image time-series for the detection and monitoring of

- slow-moving landslides”. In: *Remote sensing of environment* 189, pp. 40–55.
- Tsai, Fuan, J-H Hwang, L-C Chen, and T-H Lin (2010). “Post-disaster assessment of landslides in southern Taiwan after 2009 Typhoon Morakot using remote sensing and spatial analysis”. In: *Natural Hazards and Earth System Sciences* 10.10, p. 2179.
- Tsou, Ching-Ying, Zheng-Yi Feng, and Masahiro Chigira (2011). “Catastrophic landslide induced by typhoon Morakot, Shiaolin, Taiwan”. In: *Geomorphology* 127.3-4, pp. 166–178.
- Van Westen, CJ, Th WJ Van Asch, and Robert Soeters (2006). “Landslide hazard and risk zonation—why is it still so difficult?” In: *Bulletin of Engineering geology and the Environment* 65.2, pp. 167–184.
- Wu, Xueling, Ruiqing Niu, Fu Ren, and Ling Peng (2013). “Landslide susceptibility mapping using rough sets and back-propagation neural networks in the Three Gorges, China”. In: *Environmental earth sciences* 70.3, pp. 1307–1318.
- Yu, Bo and Fang Chen (2017). “A new technique for landslide mapping from a large-scale remote sensed image: a case study of Central Nepal”. In: *Computers & Geosciences* 100, pp. 115–124.
- Zhu, Xiaolin et al. (2016). “A flexible spatiotemporal method for fusing satellite images with different resolutions”. In: *Remote Sensing of Environment* 172, pp. 165–177.

Detecting and monitoring long-term landslides in urbanized areas with nighttime light data and multi-seasonal Landsat imagery across Taiwan from 1998 to 2017

Tzu-Hsin Karen Chen, Alexander V. Prishchepov, Rasmus Fensholt, Clive E. Sabel

Supplementary data

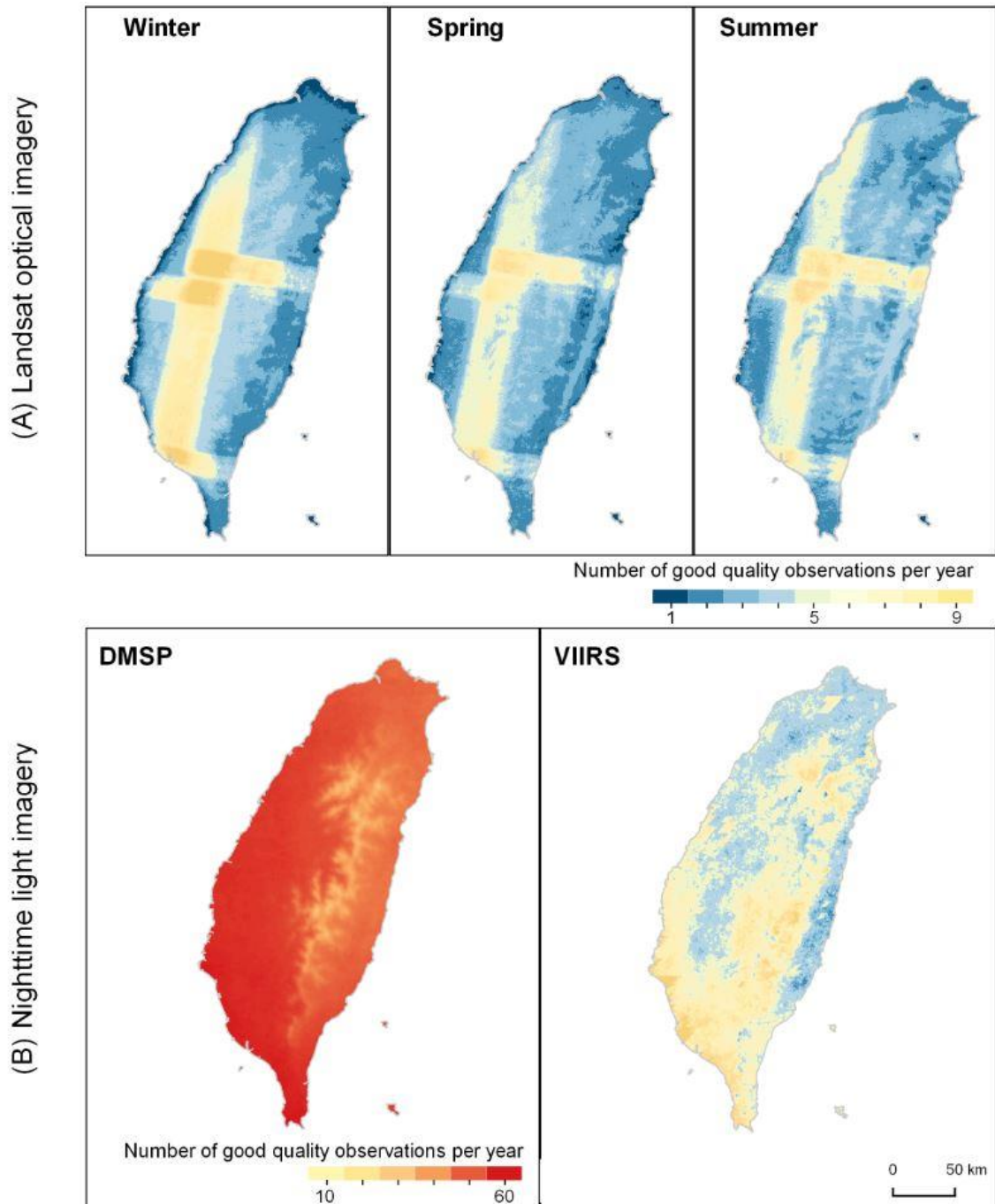


Fig. S1. The observation density of annual variables, (A) Landsat optical imagery (years 1998-2017) and (B) nighttime light imagery (DMSP for 1998-2013 and VIIRS for 2014-2017). The Landsat image availability was assessed for winter, spring, and summer. The DMSP data were annual composites and VIIRS were March composites (avoiding summer).

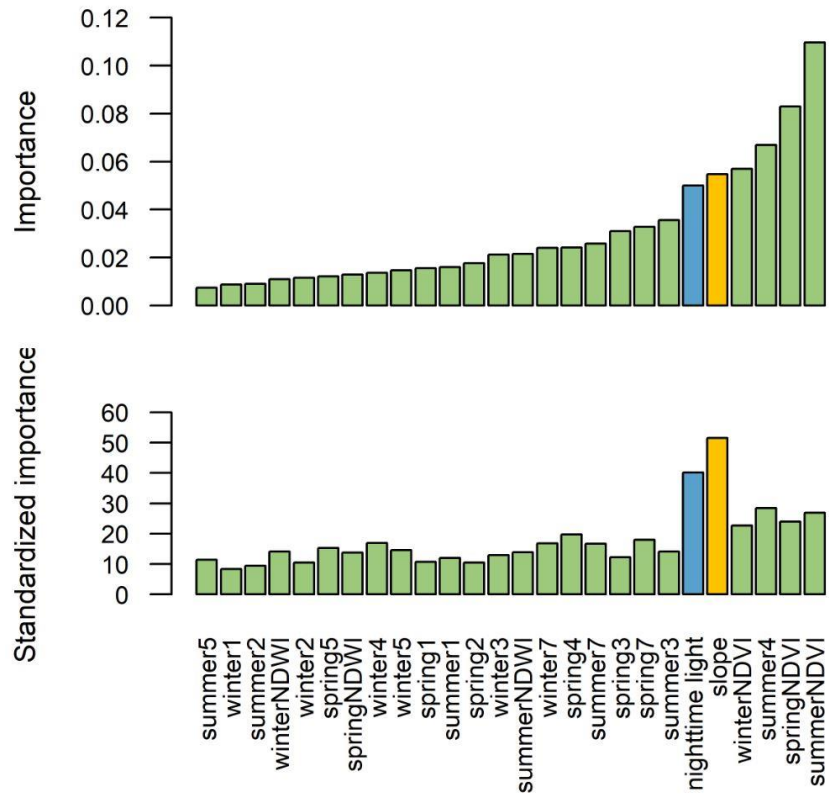


Fig. S2. The importance of a variable was measured as the mean decrease in the producer's accuracy of the landslide class, when the variable in question is excluded. Standardized (Std.) importance is adjusted by standard errors. Variables from ancillary data, nighttime light (blue) and slope (yellow), are highlighted.

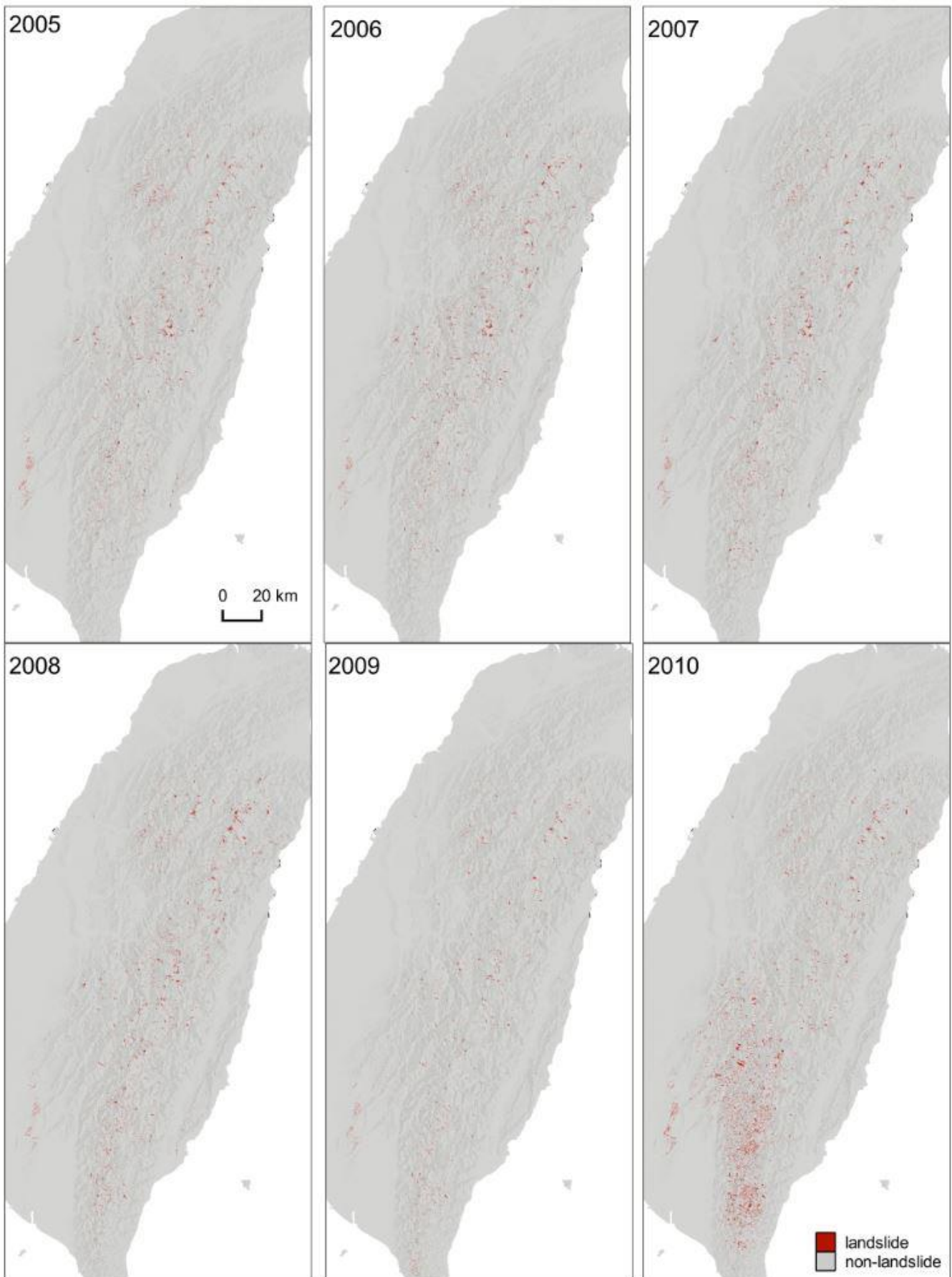


Fig. S3a. Annual reference maps 2005-2010 from the Taiwan Council of Agriculture.

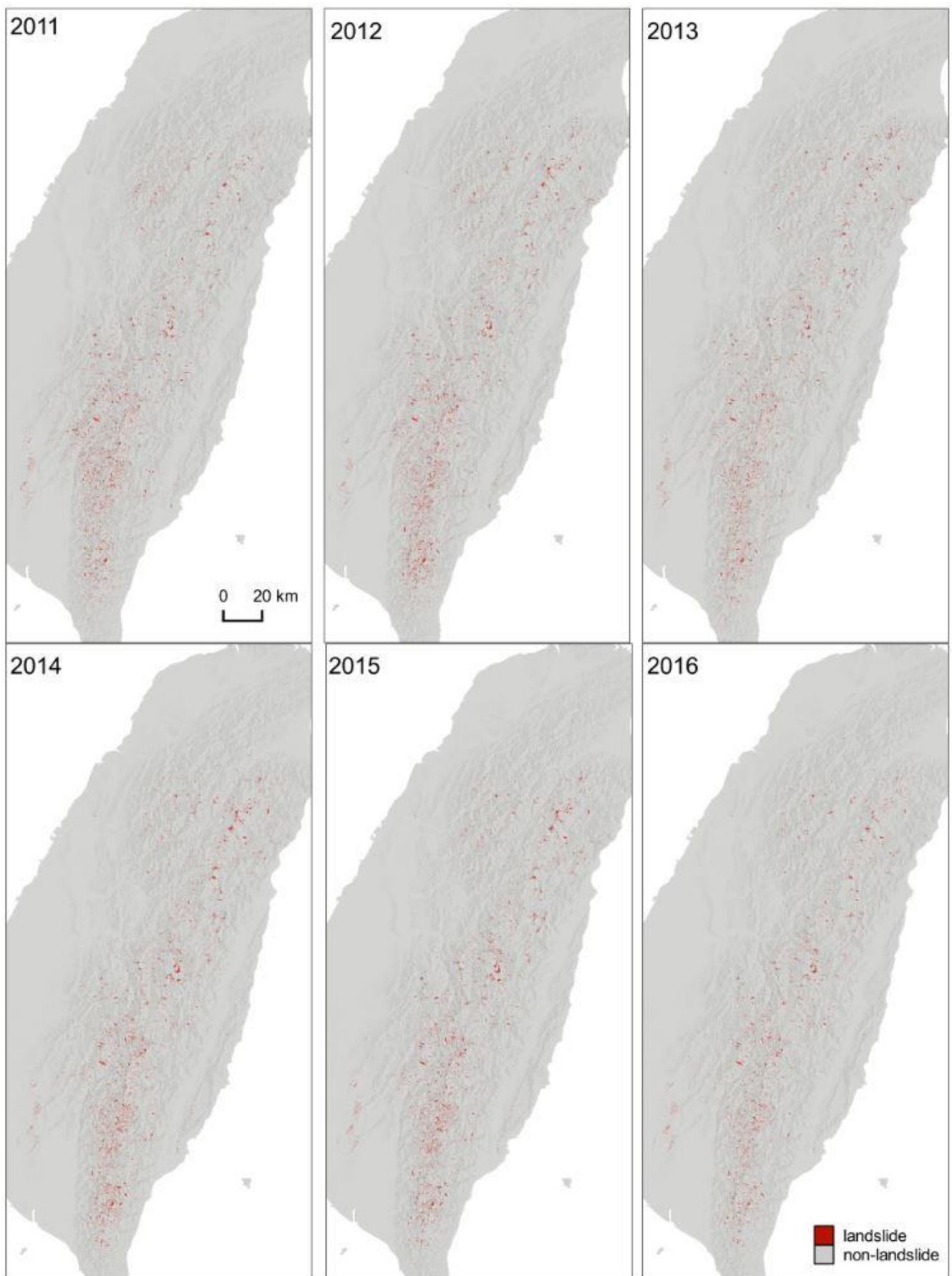


Fig. S3b. Annual reference maps 2011-2016 from the Taiwan Council of Agriculture.